ACS APPLIED NANO MATERIALS

www.acsanm.org Article

Fe_3O_4 Nanoparticles and Paraffin Wax as Phase Change Materials Embedded in Polymer Matrixes for Temperature-Controlled Magnetic Hyperthermia

Moshe Cohen-Erner,* Raz Khandadash,* Raphael Hof, Ofer Shalev, Adam Antebi, Arnoldo Cyjon, Dian Kanakov, Abraham Nyska, Glenwood Goss, John Hilton, and Dan Peer

Cite This: https://doi.org/10.1021/acsanm.1c02676 Read Online

ACCESS | Metrics & More | Article Recommendations | Supporting Information

ABSTRACT: Over the last 2 decades, magnetic hyperthermia (MH) has been recognized as a promising concept for efficient cancer treatment. Recently, it has been receiving increased attention because of its procedure simplicity, noninvasive nature, and effective solid tumor heating with minimal damage to healthy surrounding normal tissues. In this paper, we report about the development of theranostic superparamagnetic iron oxide nanoclusters, demonstrating efficient heating in hyperthermia and good response under a magnetic resonance imaging (MRI) scan. Multiple cores of 25 ± 2 nm superparamagnetic iron oxide (Fe_3O_4) nanoparticles and paraffin wax based on 24-hydrocarbon chains (tetracosane), used as a phase change material, were coencapsulated in an interior core of a self-assembled PEO−PPO−PEO polymer and subsequently covalently coated by 20 kDa branched poly(ethylene glycol), resulting in 135 ± 10 nm hydrodynamic diameter nanoclusters. The synthesized nanoclusters were found to have good stability in phosphate-buffered saline. The physicochemical and magnetic properties of the nanoclusters exhibit an efficient magnetic-to-thermal energy conversion with self-regulation of the hyperthermia temperature. Under irradiation to an alternating magnetic field (AMF) of 33 kA/m at a frequency of 300 kHz, the nanoclusters demonstrate a specific absorption rate (SAR) of 475 ± 17 W/g. The nanoclusters also exhibit a high transverse relaxivity of 68 $(mM\ s)^{-1}$ at 1.5 T MRI. In preclinical studies, nanoclusters were intravenously injected to mice bearing 4T1 triple negative breast carcinoma lung metastases. Mice were irradiated by an AMF to demonstrate the antitumor efficacy, with 66% reduction in the number of metastases, which pave the route for the application of effective hyperthermia treatment for a metastatic cancer model.

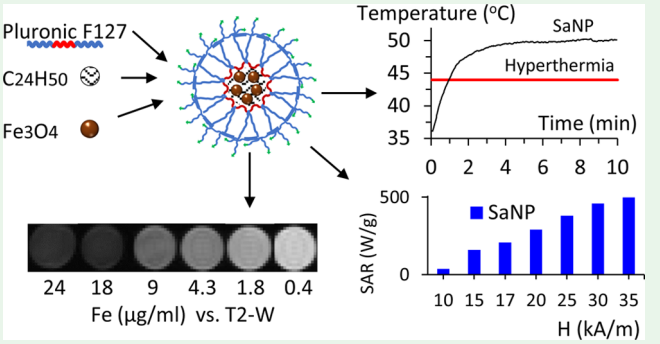

KEYWORDS: *magnetic hyperthermia, nanoclusters, phase change material, superparamagnetic iron oxide nanoparticles, specific absorption rate, theranostic, magnetic resonance imaging*

1. INTRODUCTION

Lung cancer is one of the most aggressive types of cancer worldwide.[1] The aggressive invasiveness characteristics of lung cancer contribute to the short-term survival of patients and present a therapeutic challenge. Significant advances have been made in cancer therapy, although the selective elimination of cancer cells remains challenging. Therefore, it is vital that effective methods for selective treatment with improved safety and efficacy are developed to enhance conventional methods that will prolong survival, control symptoms, and improve patients' quality of life.

One of the promising therapeutic technologies for cancer treatment is hyperthermia. Heat exposure of malignant cancer cells to temperatures between 42 and 46 °C for at least 30 min leads to apoptosis *in vivo* and *in vitro*, rendering it a preferable strategy for tumor eradication compared to the necrosis mechanism occurring at temperatures above 46 °C.[1] Moreover, at this temperature range, tumor cells are more sensitive to heat than normal cells. This phenomenon is related to the complex vasculature architecture of solid tumors, which includes hypoxic and low-pH regions.[2]

Magnetic hyperthermia (MH) and photothermal therapy (PTT) techniques are widely explored innovative cancer hyperthermia therapies that elevate the local malignant tissue temperature by heat generation, using the magnetic and optical

Received: August 30, 2021
Accepted: September 20, 2021

characteristics of distinct or composite nanoentities. These nanoentities are located within, or stay close to, the tumor lesion and induce cell death upon exposure to a noninvasive external force such as a magnetic field or near-IR−IR radiation.[3] Unlike the PTT used to treat superficial solid tumors that are up to the depth of 3−4 mm from the skin surface,[4] MH can deal with deep-seated tumors and metastases because of the excellent tissue penetration ability of an alternating magnetic field (AMF).[5] Clinical research developments demonstrated the feasibility of MH, using 12 nm superparamagnetic iron oxide (Fe_3O_4) nanoparticles (SPIONs) activated by AMF of 2.5−18 kA/m at a frequency of 100 kHz, as a safe and effective stand-alone therapy for prostate carcinoma[6] and glioblastoma multiforme (GBM).[7] These results were further corroborated by phase 2 clinical trials, examining the MH technique as a GBM adjuvant therapy.[8] Despite the main advantage of this technique to easily treat localized and superficial, or easily accessible, tumors without damaging healthy tissue, this approach is limited to specific types of cancer and is not applicable to a cancer in advanced stage. Furthermore, direct tumor injection results in a nonhomogeneous SPION distribution within the tumor, which makes complete regression of the tumor difficult and entails a high risk of metastasis development, unsuitable for local conventional MH treatment. These drawbacks can be overcome by the systemic delivery of magnetic nanoparticles (MNPs) through intravenous (IV) administration. This allows the technique to be employed in tumors in various sizes, locations, and distribution.[9]

Previous reports suggest that the relatively moderate heating efficiency of SPIONs, indicated by the specific absorption rate (SAR) parameter, combined with their low tumor accumulation, presents some limitations on the clinical realization of systemically delivered MH.[9] In addition, in order to minimize potential side effects, the dosage of SPIONs administered during MH should be kept to a minimum.[10] Ideally, one would desire to increase the SAR as much as possible in order to achieve an efficient hyperthermia treatment with a low amount of SPIONs. In the last decades, different strategies have been proposed in order to synthesize SPIONs that possess enhanced SAR values while retaining their inherent benefits (e.g., biocompatibility). These schemes include tuning of the particle size, magnetic anisotropy, coating, and magnetization,[11,12] which are the parameters identified as the determinants of both the static and dynamic behavior of single-domain nanoparticles (NPs).[13] At present, most existing MNPs require a high frequency or a high AMF intensity to deliver an adequate thermal dose to the tumor, while there are clinical upper limits for the magnetic field intensity and frequency values that the human body can withstand.[14] New types of colloidal clusters composed of multicore MNPs have been developed to overcome these aforementioned drawbacks and produce higher heating rates for the same concentration of MNPs or, alternatively, obtain similar temperature rises with smaller MNP concentrations. This phenomenon was ascribed to "spin-glass" dynamics of the magnetic moments within a cluster, strongly correlated by the exchange interaction influencing the higher magnetic susceptibility at low magnetic field strength.[14] This has significance for MH applications, where the SAR in the currently studied materials has not been sufficiently high at reasonable concentrations to target small tumors.[15] Thus, the ability to achieve temperature rises at lower concentrations allows for novel means of MNP delivery to the tumor site by IV administration. Moreover, the translational research of MH with systematically administrated NPs is limited because of the lack of a control mechanism over temperature rises of the NPs, in both healthy and cancer tissues, upon exposure to an AMF.[16]

Recently, we proposed a new method to control and regulate the temperature of NPs in tissues by using tetracosane (paraffin wax) as a phase change material (PCM), incorporated in the NP structure.[17] Tetracosane was selected as a PCM to provide high latent energy and high specific heat capacity, in both liquid and solid phases, with a phase change temperature required by hyperthermia (47−53 °C), and biocompatibility with the biological tissue.[17]

In this paper, we present a MH scheme that is based on temperature-controlled SPION nanoclusters at a size of 135 ± 10 nm, activated by AMF (8−33 kA/m, 300 kHz). The nanoclusters are coencapsulating multiple 25 nm SPION cores and 275 J/g latent-heat tetracosane, which serves as a PCM.[17] Their outer shell is based on the biocompatible material poly(ethylene glycol) (PEG). We were able to demonstrate an IV administration and localization of the nanoclusters to be targeted passively on cancer cells. The nanoclusters, called Sarah nanoparticles (SaNPs), have been characterized in terms of the physiochemical properties magnetic-to-thermal conversion efficiency and energy absorption capability. Here, we present the nanoclusters used and the performance in terms of the MH efficiency and therapeutic efficacy *in vivo*.

2. EXPERIMENTAL SECTION

2.1. Materials. The 25 nm oleic acid-capped SPIONs (Fe_3O_4) were purchased from Imagion Biosystems (San Diego, CA). Poly(ethylene oxide)−poly(propylene oxide)−poly(ethylene oxide) (PEO−PPO−PEO) triblock copolymer (Pluronic F127; M_w = 12600 g/mol) was purchased from Sigma-Aldrich (Rehovot, Israel). *p*-Nitrophenyl chloroformate (*p*-NPC) (97%) and tetracosane (>99%) were purchased from Acros Organics (Carlsbad, CA, and Czech Republic). Amine-functionalized 6-arm-branched PEG (M_w = 20 kDa) was purchased from Sunbio Inc. (Gunpo-si, Gyeonggi-do, South Korea). Glucose [50% (w/v)] was purchased from B. Braun (Melsungen, Germany). Hydrochloric acid (HCl; 36.5−38%) and nitric acid (69−70%) for trace metal analysis were purchased from Avantor Performance Materials Inc. (Allentown, PA). All other chemicals were of analytical grade.

2.2. Synthesis of Water-Dispersible SaNP Nanoclusters. To synthesize the SaNP nanocluster, the chemically inert Pluronic F127 was first activated with *p*-NPC at its two terminal hydroxyl groups following the preparation procedure referred to in the literature.[18] The activation efficiency was determined using ^{1}H NMR. The SaNP nanoclusters comprising an inner core encapsulating SPIONs and tetracosane and a hydrophilic Pluronic F127/amine-functionalized 6-arm-branched PEG polymer shell layer were prepared using a modified emulsification/solvent evaporation method.[19] Briefly, the mixture of *p*-NPC-activated Pluronic F127 (5.2 g), tetracosane (36 mg), and oleic acid-capped SPIONs (15 mg) dissolved in 6 mL of dichloromethane (DCM) was added in a dropwise manner to the 36 mL aqueous solution (pH = 8.4) containing 93 mg of amine-functionalized 6-arm-branched PEG. The oil-in-water mixture was then sonicated using a 20 kHz Vibra cell ultrasonication (VCX-750) for 4 min followed by pH neutralization of the solution with 37% HCl (120 μL) to quench the reaction. The organic solvent (DCM) in the emulsion was then removed by rotary evaporation with a water bath set at 40 °C until the solution became clear. The resultant dispersion containing the SaNP nanoclusters was washed several times by centrifugation [4 h at 18000 relative centrifugal force (rcf)]−precipitation−redispersion cycles using water for irrigation (WFI) and filtered through a sterile 0.22 μm filter (Sartorius, Israel). After

https://doi.org/10.1021/acsanm.1c02676
ACS Appl. Nano Mater. XXXX, XXX, XXX−XXX

filtration, the SaNP nanoclusters underwent additional centrifugation (2 h at 14000 rcf) in order to concentrate the final product followed by aseptic filling. In the preclinical studies, the SaNP nanocluster dispersion was diluted with 50% (w/v) glucose to produce an isotonic solution (5% glucose concentration).

2.3. SaNP Nanocluster Characterization. The hydrodynamic diameter, ζ potential (ZP), and polydispersity index (PDI) of the obtained SaNP nanoclusters were determined by a Zetasizer Nano Series ZS (Nano-ZS, Malvern Instrument Ltd., Malvern, Worcestershire, U.K.). The nanocluster morphology was characterized by a Tecnai G2 cryogenic transmission electron microscopy (cryo-TEM) system. The total mass and iron content in the synthesized nanoclusters was determined using an atomic absorption spectrometry (AAS) analysis. The SaNP nanocluster concentration (mg/mL) in the purified aqueous dispersion was determined by weighing the remaining solid after water was removed from a given dispersion volume by a lyophilization process using a Labconco FreeZone benchtop freeze-dry system (−105 °C; 4.5 L). The ratio of organic-to-inorganic material in the SaNP nanocluster formulation in a given volume was calculated by subtracting the SPION mass determined by AAS from the dry weight of SaNP nanoclusters obtained after a dry-freezing process. The chemical composition of the SaNP nanocluster was characterized with a Nicolet 8700 spectrometer fitted with a deuterated triglycine sulfate detector (Thermo Scientific Inc., Waltham, MA) and equipped with an attenuated-total-reflectance accessory with a diamond crystal. The magnetization curves of nanoclusters were determined with a superconducting quantum interference device (SQUID; Quantum Design MPMS) at room temperature. The magnetic fluid heating experiments were performed with a 6.6 kW high-frequency induction heating system model WUH-06A (Shenquia Yongda High Frequency Equipment Co., Inc., Zhoukou, China), which could generate an AMF at a frequency of 290 kHz ± 10%. For the SAR measurement, the average slope of the temperature versus time plot during the first 2 min of heating was drawn and the heating rate was calculated by forward linear fitting of each sample, using the first 30 s data, and subtracted by that of the solvent alone to compensate for the heat exchange with the environment. The SAR was calculated using eq 1. Detailed characterization procedures are provided in Notes S1−S7.

2.4. SaNP Nanocluster Stability Study in Physiological Media over Time. A stability study of SaNP nanoclusters in physiological media was carried out using 6 mL of SaNP nanoclusters dispersed in WFI, concentrated to 2 mg/mL (2 h of centrifugation at 14000 rcf), conducted in a class-10000 clean-room facility. The solution is then resuspended in 6 mL of Dulbecco's phosphate-buffered saline (PBS) under aseptic conditions. The SaNP nanoclusters were transferred into 10 mL glass vials [OMPI, Stevanato group] sealed with rubber stoppers (West) and aluminum caps (West) to avoid contamination of the samples during the incubation period. Finally, the SaNP nanoclusters were stored for 14 days at controlled temperatures of 15−25 °C and humidity of 50−60%. Analyses for hydrodynamic size, ZP, and heating rate measurements were carried out at two time points, 7 and 14 days after start, and compared to those measured at the starting point (control).

2.5. Evaluation of SaNP Nanocluster Detection by Magnetic Resonance Imaging (MRI). *In vivo* biodistribution of IV-administered SaNP nanoclusters was determined using MRI modality. It is used to characterize the SPION accumulation in vital organs and to adjust the optimal dosage (mg/kg) in the body. MRI tests were conducted on a 1.5 T whole-body MRI scanner (Optima MR-450W, GE Healthcare's Premium 1.5 T, 70-cm-wide bore MRI system). A 32-channel anterior array coil was used to scan the torso part of 32 cm length. T_2-weighted images were acquired using a multislice, multiecho pulse sequence. The scan parameters are 33 axial slices placed in a field of view of 320 mm, an image spatial resolution of 256 × 256 pixels (350 mm × 350 mm), a slice thickness of 7.5 mm, and a slice spacing of 2.5 mm. T_2 weighting was obtained using a repetition time (T_R) of 3000 ms and eight echo times (T_E = 9.7, 19.4, 29.1, 38.8, 48.5, 58.2, 67.9, and 77.6 ms). The total scan time was 13 min. The T_2-weigthed images were analyzed using a region-of-interest tool (*ImageJ* software). The relaxation rate values ($1/T_2$) were plotted versus the SPION concentrations in the dilutions. The relaxivity was determined by a linear fit.

2.6. Cell Culture. The 4T1 triple negative breast cancer (TNBC) mouse mammary carcinoma cell line was obtained from the American Type Culture Collection (Rockville, MD). Cells were grown in an RPMI 1640 medium supplemented with 10% (v/v) fetal bovine serum, 1.0 mM sodium pyruvate, 100 U/mL penicillin, and 100 μg/mL streptomycin. Cells were maintained in a humidified atmosphere containing 5% CO_2 at 37 °C. To generate a metastatic lung cancer model, mouse 4T1 TNBC cells were grown to 70% confluency and metastatic tumors were established by harvesting early-passage 4T1 TNBC cells with 0.25% trypsin−ethylenediaminetetraacetic acid, which were centrifuged at 500*g* for 5 min and resuspended in ice cold Hanks' Balanced Salt Solution at 2.5×10^4 cells/200 μL of solution. The cell suspension was IV-injected via the lateral tail vein of BALB/c mice.

2.7. Animals. BALB/c mice, 7−8 weeks old, were purchased from Envigo (Nes-Ziona, Israel). All animal experiments were reviewed and approved by an Institutional Animal Care and Use Committee and followed officially approved procedures for the care and use of laboratory animals, and all protocols met the requirements of the local ethical committee of Technion—Israel Institute of Technology, Haifa, Israel (ethical approval No. IL-0800617). Swine of 45 kg weight, one male and two females, were purchased from Trakia University (Stara Zagora, Bulgaria). The animal handling was compliant with guidelines of the National Institute of Health (NIH). All animals were euthanized at the end of the experiments.

2.8. Evaluation of the Therapeutic Efficiency of Systemic *In Vivo* Magnetic Heating Therapy. A total of 18 BALB/c female mice, in a bearing lung metastasized 4T1 TNBC model, were weighted and randomly divided into three groups (n = 6). Each group received a different treatment: first group, 5% glucose solution; second group, SaNP + AMF (f = 300 kHz; H = 10.4 kA/m); third group, SaNP + AMF (f = 300 kHz; H = 13 kA/m). To evaluate the MH efficiency of SaNP nanoclusters with AMF application, groups 2 and 3 were IV-bolus-injected with aqueous dispersions of SaNP nanoclusters diluted with 5% glucose at a dose of 20 mg/kg in terms of mass of fraction Fe_3O_4, using an insulin syringe and a 27 G needle. Group 1 was IV-injected with 5% glucose and used as the control. A total of 8 h postinjection, groups 2 and 3 were exposed, for a 30 min time period, to continuous 300 kHz AMF at strengths of 10.4 and 13 kA/m, respectively. The treatment was composed of three repeated MH cycles, at the 14th, 16th, and 18th days after cell inoculation. At the 21st day, the animals were sacrificed, followed by lung excision and visual counting of the number of metastasis nodules and by histopathology efficacy evaluation. The number of tumors/nodules in the lungs was reported, expressed as either single or multiple nodules. A two-dimensional (2D) morphometric measurement and an average area quantitation (mm^2) were done on the largest nodule (i.e., tumor) in the lung sections. The morphometric evaluation was performed using the Augmentiqs system (https://www.augmentiqs.com/).[20]

For the large animal preclinical study, swine, weighing ∼10 kg, were IV-administered with a dose of 2.6 mg/kg. Then, 4 h postinjection, they were subjected to AMF application using a clinical system with an AMF strength of 12 kA/m at a frequency of 300 kHz. The AMF application was conducted in the target area, which included the heart, lungs, stomach, liver, spleen, and kidneys. The irradiated animals were monitored for 5 days after AMF exposure. The follow-up included monitoring of the clinical signs and behavioral changes and blood and coagulation analyses.

2.9. Histopathology Analysis. Histological slides were prepared by Patho-Logica Laboratory, Nes-Ziona, Israel. Tissues harvested for microscopic examination were fixed in 4% formaldehyde. Tissues were trimmed in a standard position and sectioned into five different longitudinal cross sections with an interval of 100 μm each. Per lung, five cross-sectional levels were prepared [#1 (most dorsal level), #2 (dorsal level), #3 (middle level), #4 (ventral level), and #5 (most ventral level)], mounted on glass slides, and stained with hematoxylin and eosin (H&E).

https://doi.org/10.1021/acsanm.1c02676
ACS Appl. Nano Mater. XXXX, XXX, XXX−XXX

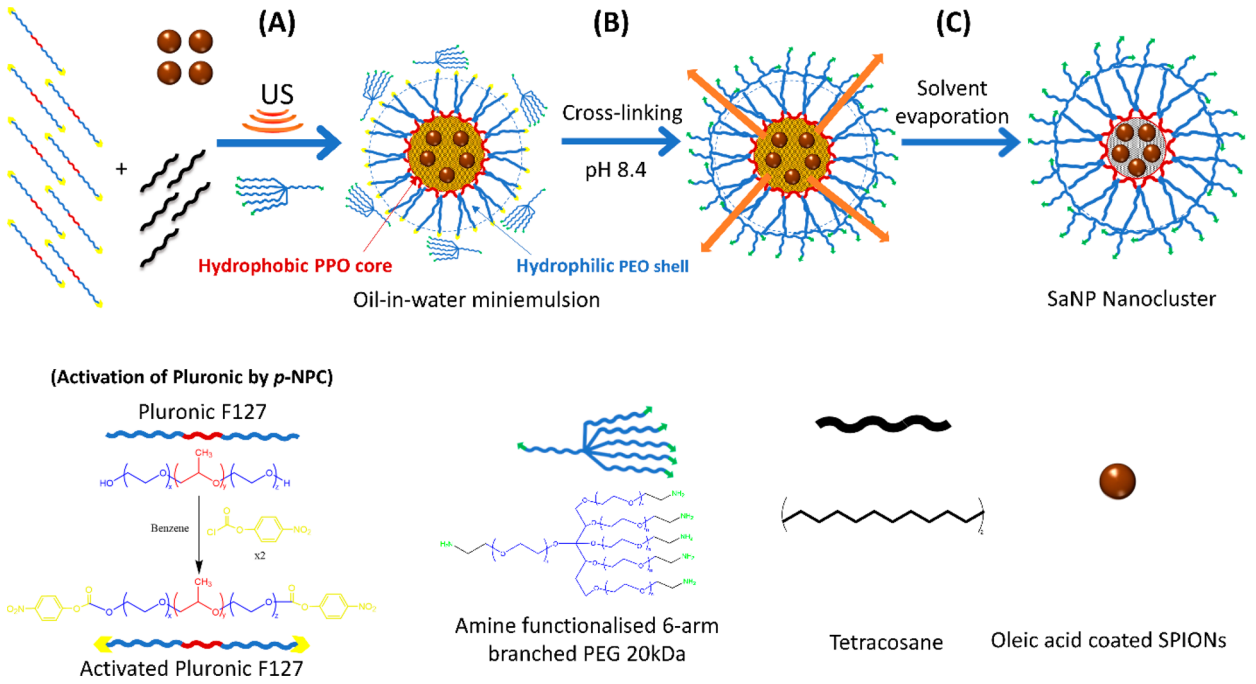

Figure 1. Illustration of the chemistry and procedures to synthesize the SaNP nanoclusters. (A) Ultrasonic (US) emulsification of an organic oil phase mixture of a *p*-NPC-activated PEO−PPO−PEO copolymer, tetracosane, and SPIONs in an aqueous phase. (B) Shell cross-linking between the PEO−PPO−PEO and PEG polymers. (C) Solvent evaporation to form SaNP nanocluster encapsulation of SPIONs and tetracosane and a hydrophilic amine-functionalized 6-arm-branched PEG polymer shell layer.

2.10. Statistical Analysis. All data are expressed as the mean ± standard deviation. The statistical significance of the differences between groups was analyzed by a Student's *t* test, and a *p* value of <0.05 was considered to be statistically significant. A comparison of the results among groups was carried out by one-way analysis of variance (ANOVA).

3. RESULTS AND DISCUSSION

3.1. Design and Synthesis of PEGylated SPION-Based Nanoclusters for Temperature-Controlled MH. Enhanced SAR for MH applications is a challenge that has been addressed by many studies over the years.[21−23] Recently, magnetic nanoclusters consisting of SPION cores codoped with zinc/manganese or cobalt/manganese[24] were demonstrated to be used as heat mediators for systemically delivered MH because of their high heating efficiency. However, this approach does not stand in line with regulatory safety requirements related to a clinical use of NPs containing heavy metals in their structure. There is currently insufficient data concerning the exposure and degradability of heavy-metal NPs *in vivo*. SPIONs have been explored traditionally for application in MH because of their biocompatibility and biodegradability.[25] Moreover, SPIONs with sizes within the range of 20−40 nm were demonstrated to have high SAR values when irradiated by an AMF at a frequency range of 325−341 kHz.[26−28] In an attempt to develop biocompatible IV systemic delivered nanoclusters comprising both high heating efficiency and controllable temperature functionality, we synthesized a new class of NPs that contain tetracosane and multiple cores of narrow-sized spherical-shaped 25 nm SPIONs coated with oleic acid in their reservoir structure and are functionalized with PEG at their outer surface. Tetracosane is a paraffin wax-based material with 24 carbon atoms in its backbone. Because of its high latent heat of fusion, obtained by undergoing a phase change, >275 J/g, we used it as a PCM component of SaNP nanoclusters to enable control of the NP temperature within the range of 47−53 °C.[29]

A PEO−PPO−PEO block copolymer, which undergoes self-assembly in aqueous media, was used to encapsulate tetracosane and SPIONs to form highly stable aqueous nanocapsules. It also serves as a delivery vehicle of tetracosane and SPIONs through the surrounding medium by using its well-known ability to facilitate solubilization of poorly water-soluble materials in drug-delivery systems.[30] Above the critical micelle temperature and concentration, the PEO−PPO−PEO copolymer spontaneously forms polymeric micelles with a distinct core−shell structure in which a hydrophobic inner core (PPO middle block) is surrounded by a hydrophilic shell (PEO flank blocks) exposed to the water phase. The PPO core can incorporate water-insoluble molecules and protects the interior agent from exterior components.[31] Therefore, tetracosane and SPIONs (the water-insoluble components) were loaded into the hydrophobic interior of PEO−PPO−PEO polymeric micelles, while the outer hydrophilic shell of the micelles (PEO flank blocks) preactivated with amine reactive moieties was cross-linked with an amine-functionalized 6-arm-branched PEG (Figure 1). The SaNP nanoclusters were prepared according to the previously reported emulsification/solvent evaporation approach,[19] confirmed as an efficient encapsulation strategy of poorly water-soluble drugs/materials into the water-soluble PEO−PPO−PEO-based polymeric nanoplatform. Briefly, this approach is based on the dispersion of a mixture containing hydrophobic components (tetracosane and SPIONs) and a *p*-NPC-activated PEO−PPO−PEO copolymer in DCM and, subsequently, emulsification in a basic buffered aqueous solution containing an amine-functionalized 6-arm-branched PEG (M_w = 20 kDa) by ultrasonication to form an oil-in-water emulsion (Figure 1A).

https://doi.org/10.1021/acsanm.1c02676
ACS Appl. Nano Mater. XXXX, XXX, XXX−XXX

The terminal groups of the PEO−PPO−PEO copolymers preactivated with *p*-NPC were conjugated covalently with the primary amine groups of an amine-functionalized 6-arm-branched PEG polymer at the interface of oil-in-water emulsion droplets to generate stable carbamate bonding, resulting in shell cross-linking between the PEO−PPO−PEO and PEG polymers (Figure 1B). Once the residual DCM was evaporated, the SaNP nanocluster, with an inner core composed of PPO segments of PEO−PPO−PEO encapsulating SPIONs and tetracosane and a hydrophilic amine-functionalized 6-arm-branched PEG polymer shell layer, was formed (Figure 1C). Following the filtration process of nonencapsulated hydrophobic large aggregates of tetracosane and free oleic acid-capped SPIONs, a stable SaNP nanocluster dispersion in water was obtained.

3.2. MH Temperature-Controlled by PCM. To verify the temperature-controlled property, the magnetic-to-thermal conversion behavior of SaNP nanoclusters was evaluated by continuously applying AMF irradiation with a field amplitude of 33.4 kA/m at 300 kHz for 30 min. The sample was thermally equilibrated to a stable 36.5 ± 0.5 °C temperature range for 3 min to simulate a human core temperature prior to the application of AMF irradiation. Care was taken to set stable and close-to-adiabatic conditions of the test sample with the environment.[32]

Figure 2 illustrates the temperature profiles of water-dispersible individual 25 nm SPION particles and SaNP nanoclusters for two different SPION concentrations, 1.81 and 2.56 g/L. We found that the heating rate was higher for higher SPION dispersion concentration.[33]

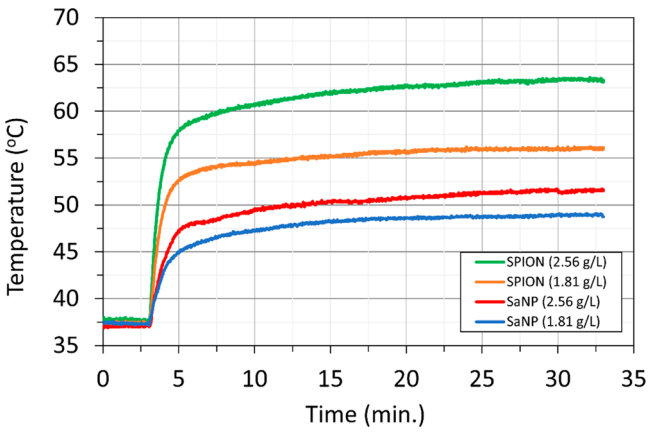

Figure 2. Temperature profiles of SaNP nanoclusters versus PEGylated SPIONs, demonstrating PCM functionality for controlling the thermodynamic equilibrium temperature under continuous AMF irradiation (33.4 kA/m at a frequency of 300 kHz).

For the reference line, the heating profile of individual 25 nm PEGylated SPIONs was measured. In Figure 2, the thermal equilibrium temperatures of SPION solutions over 30 min of continuous AMF irradiation were found to be 56 °C (orange line) and 63 °C (green line) for concentrations of 1.81 and 2.56 g/L, respectively. Thus, with a higher concentration, a higher equilibrium plateau temperature is reached.

To demonstrate the PCM functionality, SaNP nanocluster samples were heated under the same setup. The profiles shown in Figure 2 (blue and red lines) depict the temperature plateaus within the range of 48−52 °C, independent of their SPION mass contents. These profile plateaus are in agreement with the melting-phase-transition temperature range of the tetracosane component.[28] The water temperature for both SaNP nanocluster samples reached 47 °C, the phase-change melting onset of tetracosane, within 2−3 min from the start and moderately increased to around 48−52 °C. The absence of a phase-transition temperature peak above 52 °C in the SaNP nanocluster profiles confirms that the solid-to-liquid phase transition was not completed and tetracosane indeed remained in its solid−liquid state, acting as a PCM temperature control.

The PCM also shows good reversibility of energy storage and release. Magnetic-to-thermal energy conversion cycling tests of 10 successive heating and cooling cycles were performed using a SaNP nanocluster sample, irradiated under AMF of 33.4 kA/m and 300 kHz. Figure S1 depicts the profiles for the 1st, 5th, and 10th cycles. The profiles of the 5th and 10th heating cycles coincide with the first baseline cycle. The repeatability of this profile demonstrates the high solid-to-liquid phase-transition reversibility of tetracosane-based nanoclusters.

These results demonstrate the magnetic-to-thermal conversion of SaNP nanoclusters with a thermal heating control capability due to PCM physical properties, which is key function to allow efficient temperature control, compared to previously reported approaches, and to prevent healthy tissue overheating MH application.[34−37]

3.3. Fourier Transform Infrared (FTIR) Spectral Analysis. Attenuated-total-reflectance Fourier transform infrared (ATR-FTIR) spectroscopy analysis was performed to verify the presence of a PEO−PPO−PEO block copolymer in the SaNP nanocluster composition. The spectra are presented in Figure 3. In the tetracosane spectrum (green line plot in Figure 3), the peaks at 2958, 2922, and 2853 cm^{-1} wavenumbers are attributed to C−H stretching, the peaks at 1470 and 1376 cm^{-1} to $-CH_2$ asymmetric and $-CH_3$ symmetric deformation, and the peak at 720 cm^{-1} to $-(CH_2)_n-$ in-plane swinging. As noticed in the SaNP nanocluster spectrum (red line plot in Figure 3), the appearance of the above-mentioned spectral peak components indicates well-integration of *n*-tetracosane into the SaNP nanocluster. When the FTIR spectrum of PEO−PPO−PEO is compared to that of the SaNP nanocluster (blue and red line plots, respectively, in Figure 3), similar principal absorption peaks, mainly at 2882 cm^{-1} (C−H aliphatic stretching), 1343 cm^{-1} (in-plane O−H bending), and 1100 cm^{-1} (C−O stretching), are observed on both materials' spectra. Moreover, the presence of an asymmetric stretching band of carbonyl

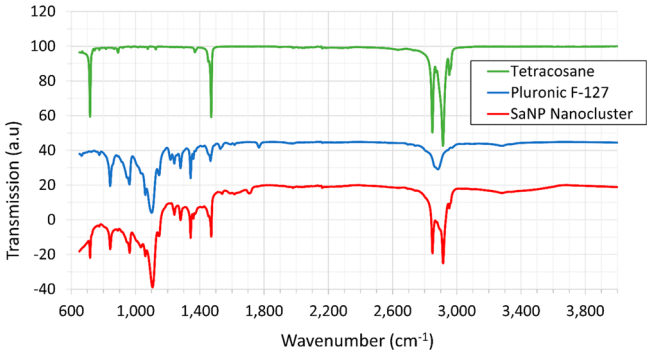

Figure 3. ATR-FTIR spectra of tetracosane, Pluronic F127, and SaNP nanocluster.

https://doi.org/10.1021/acsanm.1c02676
ACS Appl. Nano Mater. XXXX, XXX, XXX−XXX

(−CO−), located at 1704 cm^{-1}, is noticeable only for the SaNP nanocluster, indicating the formation of carbamate bonding. In summary, all of these observations indicate proper integration of a PEO−PPO−PEO block copolymer and tetracosane in the SaNP nanocluster composition.

3.4. SaNP Nanocluster Chemical Composition. The mass weight ratio of SPIONs to the whole freeze-dried SaNP nanocluster, evaluated by AAS analysis, is about 58 wt %. The tetracosane-to-nanocluster mass weight ratio, as found by gas chromatography/mass spectrometry analysis, is about 6 wt %. Accordingly, the weight percentage of the remaining organic content in the SaNP nanocluster composition is 36 wt %, which is attributed to the presence of a mixture of a PEG polymer and a PEO−PPO−PEO copolymer. The SPION-to-SaNP nanocluster encapsulation yield is as high as 77% (by mass). The presence of tetracosane and oleic acid-capped SPIONs within the SaNP nanocluster and its excellent water dispersibility demonstrate the core−shell structure of the SaNP nanocluster with cross-linked PEO−PPO−PEO/PEG as a shell structure. To the best of our knowledge, this is the first time that it has been reported that an efficient encapsulation of a long-chain hydrocarbon (C24) was performed to generate stable NPs.

3.5. Hydrodynamic Particle Size. The hydrodynamic size of the synthesized SaNP nanoclusters and the surface-charge ZP were characterized using dynamic light scattering (DLS). Figure 4 presents the DLS measurement, which indicates that

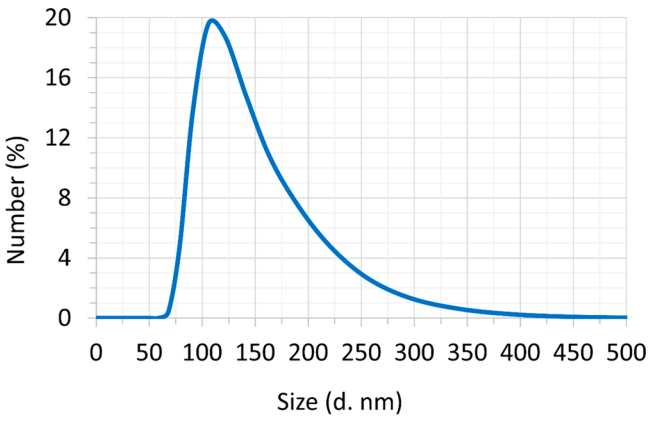

Figure 4. Hydrodynamic diameter of SaNP nanoclusters analyzed by DLS.

the synthesized SaNP nanoclusters exhibit a mean hydrodynamic diameter of 135 ± 10.5 nm with a narrow size distribution (PDI ≤ 0.15). Notably, the SaNPs' surface electric charge was measured to be a negative value (ZP = −9.7 ± 1.2 mV) at neutral pH, as depicted by Figure S4.

Generally, one should expect to observe a positive surface electric charge due to the presence of unreacted primary amines, naturally protonated at neutral pH, originating from the PEG chains of an amine-functionalized 6-arm-branched PEG polymer, which did not participate in the surface cross-linking reaction. We attribute the negative electric charge to a shift of the diffusive layer slipping plane away from the nanocluster surface; this shift is caused by the PEG polymer chains as described previously,[38] and thus the terminal amino groups presented on the PEG chains exist beyond the measurable shear plane used for ZP analysis.[39,40] These results provide indirect evidence for the chemical integration of an amine-functionalized 6-arm-branched PEG polymer at the outer layer of the SaNP nanoclusters, generating a PEGylated corona layer. This indicates that its role in the synthesis is not only a cross-linker agent but also a sterically stabilizing additive.

3.6. SaNP Nanocluster Morphology Characterization. The SaNP nanocluster morphology was evaluated by cryo-TEM analysis, which preserves the size and morphology of the polymer assemblies in the hydrated state and allows SaNP nanocluster imaging in their actual form. In cryo-TEM conditions, it was revealed that the samples consisted of well-dispersed nanosized clusters without significant aggregation, indicating that they were effectively stabilized by a cross-linked hydrophilic polymer shell in aqueous solution, as depicted in Figure S5. It was likely that the dispersion stability was partially attributed to the charge repulsion phenomena exerted by cationic amino groups present on cross-linked PEG or grafted PEG chains on the nanocapsules. Cryo-TEM analyses demonstrate a unique nanoreservoir structure of SaNP nanoclusters capable of enclosing diverse inorganic nanomaterials in the interior with a surrounding polymer shell layer. Because the shell cross-linking reaction occurs primarily at the interface of the oil-in-water emulsion droplets containing the SPIONs, it is conceivable that the encapsulation process does not affect the crystalline structure and magnetization properties as well as the size of the SPIONs. Therefore, it is safe to say that the current encapsulation process is potentially applicable for the stabilization and functionalization of a variety of inorganic nanomaterials that are poorly soluble and processable in aqueous solutions.

3.7. Magnetic Properties. The magnetization property in the SaNP nanoclusters with respect to the oleic acid-coated SPIONs was evaluated by recording the field-dependent magnetization $M(H)$ curve, using a SQUID at 298 K, as depicted in Figure S6. The SaNP nanocluster curve (blue line) presents negligible coercivity and remanence, suggesting that the superparamagnetic characteristic at room temperature is comparable to that of 25 nm SPIONs (green line), despite the large size of 130 nm for the SaNP nanocluster. The magnetic saturation, M_s (emu/g), of the oleic acid-coated SPIONs dropped from 75.2 emu/g [which was closer to that of bulk magnetite (92 emu/g)] to 56.4 emu/g (for SaNP nanoclusters) after a miniemulsion process and encapsulation in an organic matrix, with alignment to the M_s value, commonly reported in the literature.[13,24,28,41,42] The decrease in M_s (magnetic moment per weight unit) is partly attributed to the decreased effective weight fraction of the magnetic core. These results are in good agreement with the estimated organic component composition, showing 40% diminution at M_s, attributed to ∼40 wt % of the organic mass fraction in SaNP nanocluster sample, as previously described.[43]

3.8. SaNP Nanocluster Heating Potency for MH Clinical Application. The heating capability of the SaNP nanoclusters was evaluated by measuring their SAR value. Samples of 2 mg/mL were irradiated by an AMF in the range of 8−33 kA/m at a fixed frequency of 300 kHz. The SAR value (W/g) was calculated using the following equation:

$$\mathrm{SAR} = \frac{\rho_w}{C_{IO}} C_p \frac{\Delta T}{\Delta t} \quad (1)$$

where ρ_w is the water density (g/mL), C_{IO} is the SPION concentration in the dispersion, C_p is the heat capacity of water

https://doi.org/10.1021/acsanm.1c02676
ACS Appl. Nano Mater. XXXX, XXX, XXX−XXX

[J/(kg °C)], and $\Delta T/\Delta t$ is the heating rate (°C/s) in the first 30 s of AMF exposure of SaNP nanoclusters. Figures S2 and S3 depict the heating profiles for PEGylated SPIONs and the SaNP nanoclusters for various magnetic field strengths. The PEGylated SPIONs and the nanoclusters exhibit heating rates of 14−16 and 10−12 °C/min, respectively, which point to approximately an 80% energy conversion consistency. It is generally assumed that significant heating occurs only in very close vicinity of the iron oxide-based nanocluster surface.[44,45] Several works have accumulated indirect proof that, even if no macroscopic temperature changes under AMF are recorded, the local temperature at the NP surface might be significantly different from that of the surroundings. It was shown, for instance, that, even if the concentration of the MNPs at the tumor cells did not produce macroscopic heating, MNPs could induce apoptosis of the tumor cells under AMF.[45] Consequently, we estimate that, even at concentrations below 2 mg/mL of SaNP nanoclusters present in the malignant tissue, a local temperature increase of 10−12 °C/min can occur close to the vicinity of the SaNP nanocluster surface and so can potentially lead to an *in vivo* cellular heating to temperatures of 46−48 °C within 1 min after AMF radiation.[43−46]

The SAR obtained by the SaNP nanoclusters is improved and optimized by the specific design of the core material type, size, morphology, coating thickness, and magnetic properties. Additionally, the nanocluster synthesis was designed to have optimal size, ZP, and flexible morphology[16] to utilize the enhanced permeability and retention (EPR) effect efficiently, enabling accumulation of SaNP nanoclusters at the target site, with the purpose of increasing the SAR per unit volume. The SAR value was measured as a function of the AMF amplitude and is shown in Figure 5. Nanocluster samples of 200 μL

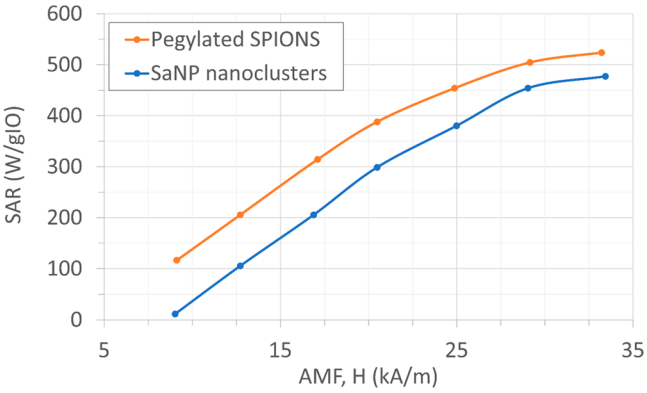

Figure 5. Evaluation of the heating profile for the nanoclusters: SAR (W/g_{SPIONs}) for SaNP nanoclusters and PEGylated SPIONs, as a function of the applied AMF.

volume, with a SPION concentration of C_{SPION} = 1.8 g/L, exhibited a heating rate of $\Delta T/\Delta t$ = 12.3 °C/min, when AMF of 33.4 kA/m at a frequency of 300 kHz was applied. Using eq 1, with a water heat capacity of C_p = 4190 J/(kg°C) and ρ_w = 1 g/mL, a SAR value of 475 ± 17 W/g_{SPIONs} was obtained. The number of SPION cores in the sample was estimated using the relationship $N = m_{SPIONs}/(\pi D^3/6)\rho_{SPIONs}$. Assuming 1 mL volume of 2 mg/mL PEGylated SPION concentration, m_{SPIONs} = 0.002 g, a diameter of D = 25 nm, and a density of ρ_{SPIONs} = 5.2 g/cm^3, we obtained a number of SPION cores of N_{SPIONs} = 4.7 × 10^{13}. In the same calculation for the SaNP nanoclusters, we took m_{SaNP} = 0.0034 g (0.002 g of SPIONs and 0.0014 g of organic contents) with D = 135 nm, and the same density of 5.2 g/cm^3 and obtained N_{SaNP} = 5.1 × 10^{11} nanoclusters. The SAR per SaNP nanocluster, SAR/N, was higher by ∼90-fold compared to the SAR per SPION core. In other words, a more efficient treatment may be attained with the nanoclusters in relation to the SPION cores per dose.

3.9. SaNP Nanocluster Stability. One of the key characteristic parameters in the design of nanoclusters is its stability over time. We tracked the SaNP nanocluster characteristics, dispersed in PBS, at three time points, analyzing their hydrodynamic diameter, ZP, and heating rate variability as a function of the storage time. No statistically significant differences were observed throughout the sampling period. Notably, the hydrodynamic size remains stable over time (Figure S7). For ZP results, SaNP nanoclusters were revealed as highly stable with no significant aggregation (Figure S8). These results provide evidence that the PEG encapsulates the SaNP nanoclusters in a way that the charged ammonium groups are exposed to the aqueous medium as mentioned earlier, which allows a robust colloidal stability to be obtained. The thermal property of SaNP nanoclusters under AMF application of 33.4 kA/m at 300 kHz was analyzed. The results in Figure 6 indicate that the heating profile and potency of the

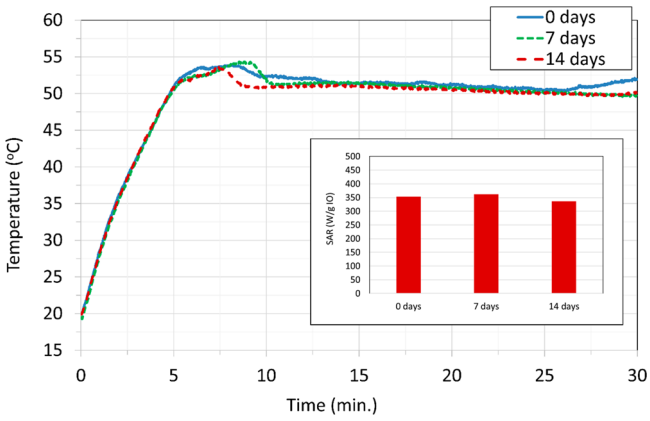

Figure 6. Heating-rate profile of SaNP nanoclusters, dispersed in PBS, analyzed by an induction heating system, before and after storage of 7 and 14 days at room temperature. The PDI parameter was found to be 0.117, 0.101, and 0.099 for storage of 0, 7, and 14 days, respectively.

SaNP nanoclusters are preserved during the storage period time. Both the good colloidal and thermal stability denote their clinical translation potential.

3.10. MH Metastatic 4T1 Breast Cancer Treatment with SaNP Nanoclusters in Mice. The SaNP nanocluster effectiveness for MH application was demonstrated in mice bearing lung metastasis through *in vivo* studies, as assessed by histopathology analysis and gross pathology nodule counting. First, we evaluated the tissue distribution of SaNP nanoclusters in mice bearing 4T1 TNBC lung metastasis (Figure S9). It was shown that SaNPs accumulate mainly in the liver and spleen, which are known to be the main reticuloendothelial system (RES) organs. The results show that 8 h nanocluster postinjection is an optimal time window for hyperthermia, while the SaNP nanocluster accumulation in normal tissue is low. In order to evaluate the MH efficacy, SaNP nanoclusters were IV-administered at a dose of 20 mg/kg to mice bearing

https://doi.org/10.1021/acsanm.1c02676
ACS Appl. Nano Mater. XXXX, XXX, XXX−XXX

4T1 TNBC lung metastasis and irradiated by AMF 8 h postinjection.

The study group was randomly divided into three groups (n = 6): group 1 was assigned as the control and injected with 5% glucose; groups 2 and 3 were injected with SaNP nanoclusters and exposed to AMF strengths of 10.4 and 13 kA/m at 300 kHz for 30 min, respectively. The treatment included of three successive cycles, with 2 days between the cycles and termination at the 8th day, sacrificing the mice for visual counting of the number of metastasized lung nodules. As can be seen in Figure 7, the average number of 4T1 TNBC metastatic pulmonary nodules for treatment group 3 (N_3 = 13 ± 8) was significantly smaller than the number found in group 1 (N_1 = 38 ± 15), which corresponded to 66% reduction in the number of metastases (p value <0.0001; Student's t test). For a moderate AMF exposure level, a similar trend of 45% reduction in the number of metastasized nodules was observed (group 2). Establishment of the primary mode of action of SaNP treatment was performed to demonstrate the effect of the incorporation of both elements SaNP and AMF, as shown in Figure S10.

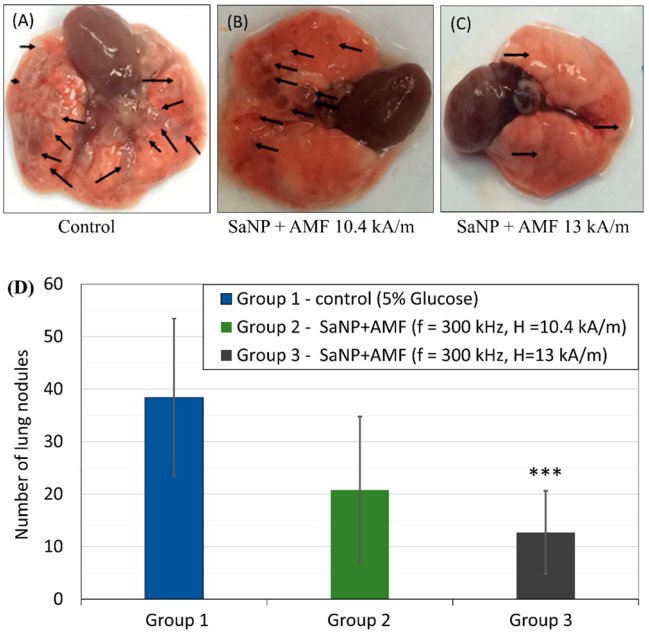

Figure 7. Three photographs depicting (by black-colored arrows) metastatic nodules in lungs: (A) untreated group as the control; (B) group treated with SaNP and AMF (amplitude application of 10.4 mT); (C) group treated with SaNP and AMF (amplitude application of 13 mT). (D) Number of metastatic lung nodules determined by gross pathology counting for each of the cases in parts A–C. (***) Statistically significant difference compared to the control (p value <0.0001). Statistical analysis was performed by the Student's t test.

To better validate the treatment impact on the pulmonary tissue, a histopathological assessment of the mice lungs was performed, using H&E staining. Histopathological assessment showed that mice treated with the SaNP nanoclusters and AMF developed a reduced number and size of metastatic nodules compared to the control group, as demonstrated in Figure 8.

A whole slide scanning and digital 2D morphometric analysis[20] of the control and treatmed mice lungs was employed to estimate the number of metastasized nodules and quantitate the percentage of metastatic surface areas in the lungs. As shown in Figure 9, the mean percentage of the lung metastatic lesion area that was found in both treatment groups 2 and 3 was measurably lower than that in the control group (17.8% ± 18.03 and 16% ± 19.66 vs 38.2% ± 14.34, respectively), indicating a reduction of 53% and 58% of the metastatic area on the lungs of treated mice groups 2 and 3, respectively. Finally, these findings were in accordance with the

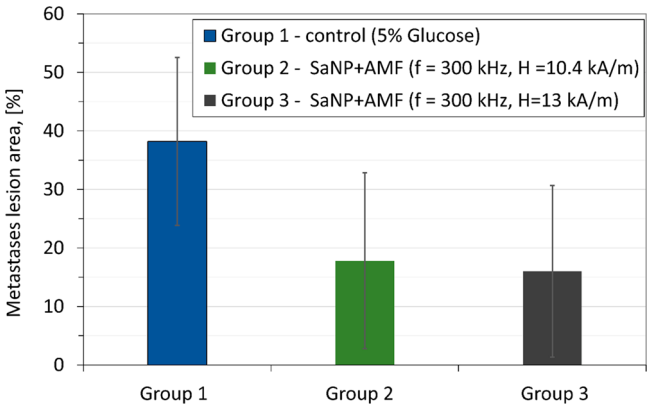

Figure 9. Percentage of metastatic lesion surface area as determined by the whole slide scanning and digital 2D morphometric analysis method.

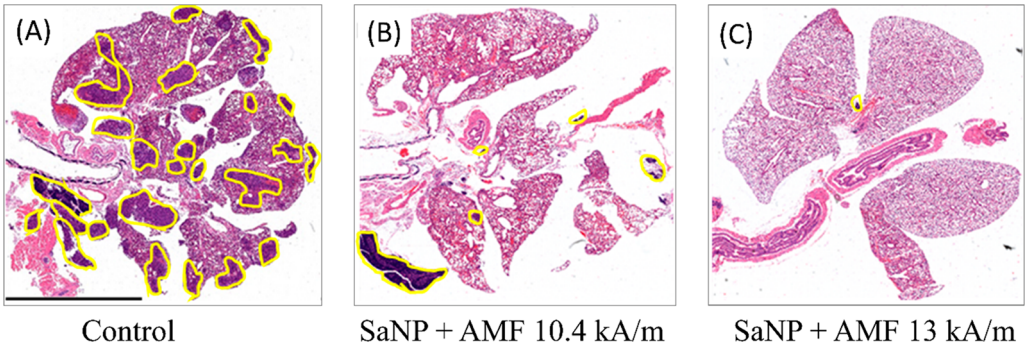

Figure 8. Representative histopathology images of lung tissues from three study groups: (A) untreated group as the control; (B) group treated with SaNP and AMF (amplitude application of 10.4 mT); (C) group treated with SaNP and AMF (amplitude application of 13 mT). H&E staining and magnification 4×. Lung tissues were removed 3 days after the last AMF cycle treatment. Tumor metastases in lung tissues are marked with yellow demarcation.

https://doi.org/10.1021/acsanm.1c02676
ACS Appl. Nano Mater. XXXX, XXX, XXX−XXX

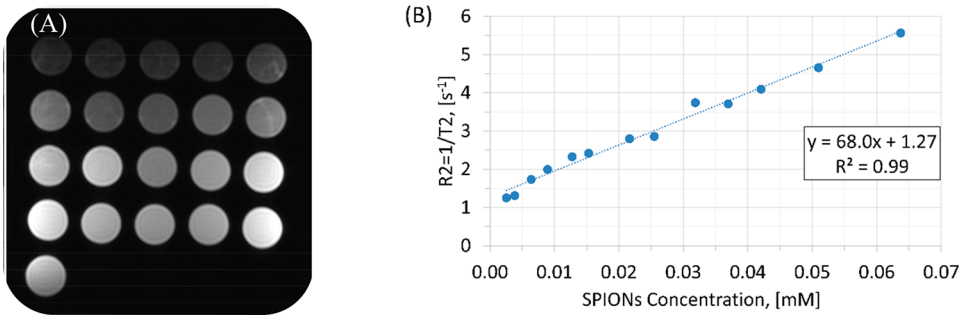

Figure 10. (A) T_2-weighted MRI image of sets of tubes containing solutions of water and SaNP nanoclusters at different SPION concentrations at 1.5T field strength. (B) T_2-weighted relaxation rates of SaNP nanocluster dispersions with various SPION concentrations. This calibration line is used to quantify the SPION concentration within *in vivo* tissue.

results obtained by the macro visual counting, suggesting that the SaNP nanocluster as a heat mediator interacts with an AMF magnetic field to induce hyperthermia to treat lung-metastasized 4T1 TNBC in a murine model.

Both groups were found with statistically significant differences compared to the control (p value <0.05). Statistical analysis was performed by the Student's t test.

3.11. SaNP Nanocluster Identification and Quantification by MRI Modality. MRI is a noninvasive technique widely used to diagnose diseases or injuries based on its high soft tissue contrast, with no penetration limit and spatial resolution.[47] MRI uses a powerful magnetic field and radio-frequency pulses to produce detailed images of organs, tissues and other internal body structures. A swine model was used to study the biodistribution of a single dose of SaNP nanoclusters, using the MRI technique, qualitatively and quantitatively.

T_2-weighted MRI enhancement by the SaNP nanoclusters was evaluated using a 1.5 T MRI scanner. T_2-weighted MRI images for different SPION concentrations of a SaNP nanocluster dispersion were acquired on the MRI instrument. Sets of tubes (50 mL volume and 30 mm diameter) filled with SPION dispersions, each at a predetermined concentration, ranging from 1:75 to 1:4000, were scanned by the MRI system using a T_2-weighted protocol. Basically, SPIONs shorten the transverse relaxation time by increasing the spin-phase coherence loss. Consequently, in the T_2-weighted image, the low SPION concentration region appears bright and the higher SPION concentration region appears darker, as shown in Figure 10A.

The plot in Figure 10B depicts the T_2-weighted mapping results. A good linear fit between the relaxation rate $R_2 = 1/T_2$ and the SPION concentration was established, demonstrating contrast variations for the different SPION concentrations. The signal intensity decays (short relaxation time) with an increase of the SPION concentration, following the equation

$$\frac{1}{T_2} = \left(\frac{1}{T_2}\right)_w + r_2 C_{\text{SPIONs}} \tag{2}$$

where $1/T_2$ is the measured relaxation rate in the presence of SPIONs, $(1/T_2)_w$ is the relaxation rate of pure water, C_{SPIONs} is the concentration of the SPIONs, and r_2 is the transverse relaxivity. Under the current system, the relaxation rate of the SaNP nanoclusters is found to be 68 $(\text{mM s})^{-1}$.

In *ex vivo* swine biodistribution studies, using a particle electron paramagnetic resonance (pEPR) technique[48] we found that SaNP nanoclusters mainly accumulated in lung, liver, and spleen tissues, the main RES organs. In order to evaluate the ability of MRI to detect the SaNP nanoclusters *in vivo* and its applicability to MH, a swine model was used, where biodistribution mapping of SaNP within the body was evaluated. Figure S11 depicts the *in vivo* MRI scan of a swine torso transverse cross section. Parts A–C of Figure S11 show the T_2-weighted mapping images that depict the preinjection, 4h postinjection, and 8h postinjection of the SaNP, respectively. The lungs are darkened 4 h after SaNP nanocluster injection (Figure S11B) as a result of the SPION presence in the lung tissue. The lungs get brighter 8 h postinjection (Figure S11C), which indicate SaNP nanocluster evacuation from the lungs.

The SaNP nanocluster biodistribution accumulation is organ-dependent and is indicated by MRI signal contrast. Quantitative analysis (unpublished experiments), based on the signals received in treated tissues, in relation to the signals from untreated tissues, shows an accumulation of more than 60%, out of the total injected volume, in the lung tissue, during the first 4 h after IV administration. This clearly points to the potential applicability of the present SaNP nanoclusters for hyperthermia clinical procedures for cancer treatment, with a special emphasis on metastases in the lungs (unpublished experiments).

3.12. Hyperthermia Procedure: Animal Model. In previous sections, we demonstrated the hyperthermia efficiency of magnetic SaNP nanoclusters on a mice model. Another preclinical study in a swine model was conducted to explore the SaNP PCM-based nanocluster thermodynamic response, the heating control management, and the potential of thermotherapeutic capability when SaNP nanoclusters are administered. The SaNP nanoclusters were IV-administered and irradiated by an AMF strength, operating within the range of 8–13 kA/m and a frequency of 300 kHz. Eight pigs, with an average weight of 10 kg, received a single dose of 2.6 mg/kg SaNP nanoclusters and were irradiated 4 h postinjection. The dose was calculated according to Food and Drug Administration guidelines.[49] Eight fiber-optic thermometry probes were located around the chest circumference, and one probe was set rectally for core body temperature recording. The core temperature was kept under control during the whole procedure within the range of 35–37 °C. Upon application of the AMF, the temperature in the metastases was estimated to reach 45–47 °C and kept stable. This averaged steady state of the tissue and body core temperature was obtained through a unique AMF irradiation profile, which was composed of three intervals with 10 min duration each and 3 min breaks. The irradiation cycle profile that was used enabled heat diffusion and conduction from the body core toward the external surface

https://doi.org/10.1021/acsanm.1c02676
ACS Appl. Nano Mater. XXXX, XXX, XXX–XXX

skin, allowing efficient heat removal by a cooling system. The thermodynamic cycling profile, as shown in Figure S12, demonstrates the controlled thermal state of the body.

To demonstrate the scalability, stability, and repeatability of the presented hyperthermia irradiation profile, a larger pig of 45 kg weight was radiated. In this preclinical study, the thermal equilibrium over 3 × 10 min cycles for a total half-hour radiation profile was demonstrated under exposure parameters of 8 kA/m at 300 kHz. Control over the thermal heat generation is depicted in Figure S13.

To evaluate the total power heat that was applied by the magnetic field on the animal's torso, the SAR induced was calculated using the relation for the absorbed power density in tissue due to eddy currents, given by

$$\mathrm{SAR} = \frac{\sigma}{2}|E|^2 = \frac{\sigma}{2}\pi^2\mu^2 r^2 f^2 H^2 \ (\mathrm{w/kg}) \tag{3}$$

where E is the induced electrical field, σ and μ are the electrical conductivity and magnetic permeability of the tissue, respectively, and r is the radial distance of the tissue from the center. f is the frequency, and H is the magnetic strength of the applied AMF. The SAR distribution within the animal body versus the radial distance was calculated and is depicted in Figure S14.

Hergt et al.[14] showed that, in order to minimize the side effects of AMF on normal tissue, the irradiated area of the human body shall be limited to a field-frequency product meeting the biological upper limit criterion of $Hf < 5 \times 10^6$ kA/(m s). Clinical studies with $Hf = 1.8 \times 10^6$ kA/(m s) (18 kA/m at 100 kHz) showed safe AMF application to GBM lesions in six 10 min sessions (60 min total treatment duration).[50] While the hyperthermia community is still discussing the safe and tolerable level of the maximum safe levels, with no clear agreement, intensive efforts have been applied by many groups to reduce eddy current heating by various strategies.[51] The frequency to field strength product used in the present *in vivo* preclinical studies was 2.4×10^6 kA/(m s) (8 kA/m at 300 kHz), which was 48% lower than the biological limit (5×10^6 kA/(m s) and showed complete control of the thermodynamic state of the pig during treatment. In the experimental setting, the core temperature profile (bold red line in Figure S12) was found to have a total increase of 1.5 °C, during the entire hyperthermia treatment without any side effects. Clinical signs or indications of complications were not observed throughout the study. Moreover, no significant hematology, chemistry, or coagulation changes were observed.

In summary, this demonstrates the ability of the high-heating-rate SPION-based SaNP nanoclusters, encapsulating PCM, to effectively enable MH treatment when the metastasis temperature was increased to 45−47 °C under the application of AMF at a controlled thermally safe level. The treatment procedure described here can be further enhanced by increasing the heating efficiency in the tumor. The SaNPs, IV-injected, target cancer cells through a passive mechanism using the EPR effect. By utilizing a glucose-based active targeting mechanism, we can potentially double the accumulated SPIONs in metastases,[52,53] due to the high glucose consumption by cancer cells, known as the Warburg effect.[54]

4. CONCLUSIONS

In summary, we have designed and synthesized safe and effective PCM-based theranostic SPION nanoclusters that offer high heating conversion efficiency in MH, with thermodynamic control and a high T_2-weighted relaxivity signal to enable the detection and quantification of SPION in organs when exposed and scanned by a MRI system. Under an irradiation to AMF of 33 kA/m at a frequency of 300 kHz, the nanoclusters demonstrated a SAR of 475 ± 17 W/g and a high transverse relaxivity of 68 $(\mathrm{mM\ s})^{-1}$ at 1.5 T. The SaNP nanoclusters presented here showed stability and integrity in terms of the physicochemical characteristics and heating profile when tested 7 and 14 days after production release. The nanoclusters also showed high heat resistivity and magnetic reversibility when subjected to multiple cycles of AMF irradiation intervals. The designed nanoclusters were used in preclinical animal studies (BALB/c mice with 4T1 TNBC tumors and large-size swine treated in a preclinical system) and found to be safe, with no toxicity effects or any adverse event findings and with highly efficient accumulation of SPIONs in cancer tumor target organs (e.g., lungs), as validated by pEPR *ex vivo* and MRI *in vivo* methods. In these preclinical studies, we demonstrated a scheme of three successive AMF irradiation intervals, with thermodynamic balance and control of the core and skin temperatures; the temperatures in the metastasized area were estimated to reach 45−47 °C, resulting in a notable reduction in the number of metastatic nodules and the cancer lesion area in mice. These nanoclusters that have shown the ability to reach the operational temperature threshold to destroy the cancer cells of tumors, using a single IV administration, have encouraged us to further advance the concept and to design a human clinical study, demonstrating the potential of MH for an efficient therapeutic treatment of cancer.

■ ASSOCIATED CONTENT

Supporting Information

The Supporting Information is available free of charge at https://pubs.acs.org/doi/10.1021/acsanm.1c02676.

Notes S1−S7 including detailed procedures for SaNP nanocluster characterization and Figures S1−S14 (PDF)

■ AUTHOR INFORMATION

Corresponding Authors

Moshe Cohen-Erner − *New-Phase Nanotechnology Ltd., Petah Tikvah 4934829, Israel*; orcid.org/0000-0001-7245-4261; Phone: +972-35411938; Email: moshece@newphase.co.il

Raz Khandadash − *New-Phase Nanotechnology Ltd., Petah Tikvah 4934829, Israel*; Phone: +972-35411938; Email: razkd@newphase.co.il

Authors

Raphael Hof − *New-Phase Nanotechnology Ltd., Petah Tikvah 4934829, Israel*

Ofer Shalev − *New-Phase Nanotechnology Ltd., Petah Tikvah 4934829, Israel*

Adam Antebi − *New-Phase Nanotechnology Ltd., Petah Tikvah 4934829, Israel*

Arnoldo Cyjon − *Oncology Department, Shamir Medical Center, Zerifin 70300, Israel*

Dian Kanakov − *Internal Noninfectious Diseases Department, Trakia University, Stara Zagora 6000, Bulgaria*

https://doi.org/10.1021/acsanm.1c02676
ACS Appl. Nano Mater. XXXX, XXX, XXX−XXX

Abraham Nyska − *Consultant in Toxicologic Pathology, Sackler School of Medicine, Tel Aviv University, Tel Aviv 69978, Israel*
Glenwood Goss − *Division of Medical Oncology, University of Ottawa, Ottawa, Ontario K1N 6N5, Canada*
John Hilton − *Division of Medical Oncology, University of Ottawa, Ottawa, Ontario K1N 6N5, Canada*
Dan Peer − *Laboratory of Precision Nanomedicine, Shmunis School for Biomedicine and Cancer Research, George S. Wise Faculty of Life Sciences, Tel Aviv University, Tel Aviv 69978, Israel;* orcid.org/0000-0001-8238-0673

Complete contact information is available at: https://pubs.acs.org/10.1021/acsanm.1c02676

Author Contributions

M.C.E. and R.K. contributed equally to this work.

Funding

This work was supported by New-Phase Nanotechnology Ltd.

Notes

The authors declare the following competing financial interest(s): M.C.E., R.K., R.H., O.S., and A.A. are employees at New-Phase Nanotechnology Ltd. The other authors declare that they do not have any affiliations that would lead to competing financial interest or any conflict of interest.

■ ACKNOWLEDGMENTS

The authors are grateful to Ricarina Rabinovitz, Ekaterina Sigalov, Pazit Rukenstein, Rana Kassem, Manzooma Kablan, Neta Buskila, Eddie Sharaga, Moshe Eltanani, Ivgeni Ram, Sasha Shlyapentokh, and Andrey Kaznasab for their generous support and contributions to this work.

■ REFERENCES

(1) Siegel, R. L.; Miller, K. D.; Jemal, A. Cancer Statistics, 2020. *CA-Cancer J. Clin.* **2017**, *67*, 7−30.
(2) Gordon, R. T.; Hines, J. R.; Gordon, D. Intracellular Hyperthermia. A Biophysical Approach to Cancer Treatment via Intracellular Temperature and Biophysical Alterations. *Med. Hypotheses* **1979**, *5*, 83−102.
(3) Siemann, D. W. The Unique Characteristics of Tumor Vasculature and Preclinical Evidence for its Selective Disruption by Tumor-Vascular Disrupting Agents. *Cancer Treat. Rev.* **2011**, *37*, 63−74.
(4) Sharma, S. K.; Shrivastava, N.; Rossi, F.; Tung, L. D.; Thanh, N. T. K. Nanoparticles-Based Magnetic and Photo Induced Hyperthermia for Cancer Treatment. *Nano Today* **2019**, *29*, 100795.
(5) Derfus, A. M.; von Maltzahn, G.; Harris, T. J.; Duza, T.; Vecchio, K. S.; Ruoslahti, E.; Bhatia, S. N. Remotely Triggered Release from Magnetic Nanoparticles. *Adv. Mater.* **2007**, *19*, 3932−36.
(6) Johannsen, M.; Gneveckow, U.; Eckelt, L.; Feussner, A.; Waldöfner, N.; Scholz, R.; Deger, S.; Wust, P.; Loening, S. A.; Jordan, A. Clinical Hyperthermia of Prostate Cancer Using Magnetic Nanoparticles: Presentation of a New Interstitial Technique. *Int. J. Hyperthermia* **2005**, *21*, 637−47.
(7) Maier-Hauff, K.; Rothe, R.; Scholz, R.; Gneveckow, U.; Wust, P.; Thiesen, B.; Feussner, A.; von Deimling, A.; Waldoefner, N.; Felix, R.; Jordan, A. Intracranial Thermotherapy Using Magnetic Nanoparticles Combined with External Beam Radiotherapy: Results of a Feasibility Study on Patients with Glioblastoma Multiforme. *J. Neuro-Oncol.* **2007**, *81*, 53−60.
(8) Maier-Hauff, K.; Ulrich, F.; Nestler, D.; Niehoff, H.; Wust, P.; Thiesen, B.; Orawa, H.; Budach, V.; Jordan, A. Efficacy and Safety of Intratumoral Thermotherapy Using Magnetic Iron-Oxide Nanoparticles Combined with External Beam Radiotherapy on Patients with Recurrent Glioblastoma Multiforme. *J. Neuro-Oncol.* **2011**, *103*, 317−324.
(9) Huang, H. S.; Hainfeld, J. F. Intravenous Magnetic Nanoparticle Cancer Hyperthermia. *Int. J. Nanomed.* **2013**, *8*, 2521−32.
(10) Dutz, S.; Hergt, R. Magnetic Nanoparticle Heating and Heat Transfer on a Microscale: Basic Principles, Realities and Physical Limitations of Hyperthermia for Tumour Therapy. *Int. J. Hyperthermia* **2013**, *29*, 790−800.
(11) Martinez-Boubeta, C.; Simeonidis, K.; Makridis, A.; Angelakeris, M.; Iglesias, O.; Guardia, P.; Cabot, A.; Yedra, L.; Estradé, S.; Peiró, F.; Saghi, Z.; Midgley, P. A.; Conde-Leborán, I.; Serantes, D.; Baldomir, D. Learning from Nature to Improve the Heat Generation of Iron-Oxide Nanoparticles for Magnetic Hyperthermia Applications. *Sci. Rep.* **2013**, *3*, 1−8.
(12) Suriyanto; Ng, E. Y. K.; Kumar, S. D. Physical Mechanism and Modeling of Heat Generation and Transfer in Magnetic Fluid Hyperthermia through Néelian and Brownian Relaxation: a Review. *Biomed. Eng. Online* **2017**, *16*, 36.
(13) Cervadoro, A.; Cho, M.; Key, J.; Cooper, C.; Stigliano, C.; Aryal, S.; Brazdeikis, A.; Leary, J. F.; Decuzzi, P. Synthesis of Multifunctional Magnetic Nanoflakes for Magnetic Resonance Imaging, Hyperthermia, and Targeting. *ACS Appl. Mater. Interfaces* **2014**, *6*, 12939−46.
(14) Hergt, R.; Dutz, S. Magnetic Particle Hyperthermia—Biophysical Limitations of a Visionary Tumour Therapy. *J. Magn. Magn. Mater.* **2007**, *311*, 187−92.
(15) Wetterskog, E.; Castro, A.; Zeng, L.; Petronis, S.; Heinke, D.; Olsson, E.; Nilsson, L.; Gehrke, N.; Svedlindh, P. Size and Property Bimodality in Magnetic Nanoparticle Dispersions: Single Domain Particles vs. Strongly Coupled Nanoclusters. *Nanoscale* **2017**, *9*, 4227−35.
(16) Pandey, S.; Quetz, A.; Aryal, A.; Dubenko, I.; Mazumdar, D.; Stadler, S.; Ali, N. Thermosensitive Ni-based Magnetic Particles for Self-Controlled Hyperthermia Applications. *J. Magn. Magn. Mater.* **2017**, *427*, 200−205.
(17) Hof, R.; Khandadash, R.; Fremder, E. Phase-Change Nanoparticle. U.S. Patent 10172939B2, 2019.
(18) Cho, K. C.; Choi, S. H.; Park, T. G. Low Molecular Weight PEI Conjugated Pluronic Copolymer: Useful Additive for Enhancing Gene Transfection Efficiency. *Macromol. Res.* **2006**, *14*, 348−353.
(19) Zhang, W.; Gilstrap, K.; Wu, L.; Bahadur, K. C. R.; Moss, M. A.; Wang, Q.; Lu, X.; He, X. Synthesis and Characterization of Thermally Responsive Pluronic F127-Chitosan Nanocapsules for Controlled Release and Intracellular Delivery of Small Molecules. *ACS Nano* **2010**, *4*, 6747−59.
(20) Zarella, M. D.; Bowman, D.; Aeffner, F.; Farahani, N.; Xthona, A.; Absar, S. F.; Parwani, A.; Bui, M.; Hartman, D. J. A Practical Guide to Whole Slide Imaging: A White Paper from the Digital Pathology Association. *Arch. Pathol. Lab. Med.* **2019**, *143*, 222−234.
(21) Lee, J. h.; Jang, J. t.; Choi, J. s.; Moon, S. H.; Noh, S. h.; Kim, J. w.; Kim, J.-G.; Kim, I. s.; Park, K. I.; Cheon, J. Exchange-Coupled Magnetic Nanoparticles for Efficient Heat Induction. *Nat. Nanotechnol.* **2011**, *6*, 418−22.
(22) Das, R.; Alonso, J.; Nemati Porshokouh, Z.; Kalappattil, V.; Torres, D.; Phan, M. H.; Garaio, E.; Garcia, J. A.; Sánchez Llamazares, J. L.; Srikanth, H. Tunable High Aspect Ratio Iron Oxide Nanorods for Enhanced Hyperthermia. *J. Phys. Chem. C* **2016**, *120*, 10086−93.
(23) Liu, X.; Zheng, J.; Sun, W.; Zhao, X.; Li, Y.; Gong, N.; Wang, Y.; Ma, X.; Zhang, T.; Zhao, L.-Y.; Hou, Y.; Wu, Z.; Du, Y.; Fan, H.; Tian, J.; Liang, X.-J. Ferrimagnetic Vortex Nanoring-Mediated Mild Magnetic Hyperthermia Imparts Potent Immunological Effect for Treating Cancer Metastasis. *ACS Nano* **2019**, *13*, 8811−8825.
(24) Albarqi, H. A.; Wong, L. H.; Schumann, C.; Sabei, F. Y.; Korzun, T.; Li, X.; Hansen, M. N.; Dhagat, P.; Moses, A. S.; Taratula, O.; Taratula, O. Biocompatible Nanoclusters with High Heating Efficiency for Systemically Delivered Magnetic Hyperthermia. *ACS Nano* **2019**, *13*, 6383−95.
(25) Sun, C.; Du, K.; Fang, C.; Bhattarai, N.; Veiseh, O.; Kievit, F.; Stephen, Z.; Lee, D.; Ellenbogen, R. G.; Ratner, B.; Zhang, M. PEG-

Mediated Synthesis of Highly Dispersive Multifunctional Superparamagnetic Nanoparticles: Their Physicochemical Properties and Function. *ACS Nano* **2010**, *4*, 2402−2410.
(26) Tong, S.; Quinto, C. A.; Zhang, L.; Mohindra, P.; Bao, G. The Size-Dependent Heating of Magnetic Iron Oxide Nanoparticles. *ACS Nano* **2017**, *11*, 6808−16.
(27) Vreeland, E. C.; Watt, J.; Schober, G. B.; Hance, B. G.; Austin, M. J.; Price, A. D.; Fellows, B. D.; Monson, T. C.; Hudak, N. S.; Maldonado-Camargo, L.; Bohorquez, A. C.; Rinaldi, C.; Huber, D. L. Enhanced Nanoparticle Size Control by Extending LaMer's Mechanism. *Chem. Mater.* **2015**, *27*, 6059−6066.
(28) Lanier, O. l.; Korotych, O. I.; Monsalve, A. G.; Wable, D.; Savliwala, S.; Grooms, N. W. F.; Nacea, C.; Tuitt, O. R.; Dobson, J. Evaluation of Magnetic Nanoparticles for Magnetic Fluid Hyperthermia. *Int. J. Hyperthermia* **2019**, *36*, 686−700.
(29) Sarı, A.; Alkan, C.; Döğüşcü, D. K.; Kızıl, Ç. Micro/Nano Encapsulated n-Tetracosane and n-Octadecane Eutectic Mixture with Polystyrene Shell for Low-Temperature Latent Heat Thermal Energy Storage Applications. *Sol. Energy* **2015**, *115*, 195−203.
(30) Russo, E.; Villa, C. Poloxamer Hydrogels for Biomedical Applications. *Pharmaceutics* **2019**, *11*, 671.
(31) Bohorquez, M.; Koch, C.; Trygstad, T.; Pandit, N. A Study of the Temperature-Dependent Micellization of Pluronic F127. *J. Colloid Interface Sci.* **1999**, *216*, 34−40.
(32) Fortin, J.-P.; Wilhelm, C.; Servais, J.; Menager, C.; Bacri, J.-C.; Gazeau, F. Size-Sorted Anionic Iron Oxide Nanomagnets as Colloidal Mediators for Magnetic Hyperthermia. *J. Am. Chem. Soc.* **2007**, *129*, 2628−2635.
(33) de la Presa, P.; Luengo, Y.; Multigner, M.; Costo, R.; Morales, M. P.; Rivero, G.; Hernando, A. Study of Heating Efficiency as a Function of Concentration, Size, and Applied Field in γ Fe2O3 Nanoparticles. *J. Phys. Chem. C* **2012**, *116*, 25602−10.
(34) Ito, A.; Tanaka, K.; Kondo, K.; Shinkai, M.; Honda, H.; Matsumoto, K.; Saida, T.; Kobayashi, T. Tumor Regression by Combined Immunotherapy and Hyperthermia Using Magnetic Nanoparticles in an Experimental Subcutaneous Murine Melanoma. *Cancer Sci.* **2003**, *94*, 308−313.
(35) Ortgies, D. H.; Teran, F. J.; Rocha, U.; de la Cueva, L.; Salas, G.; Cabrera, D.; Vanetsev, A. S.; Rähn, M.; Sammelselg, V.; Orlovskii, Y. V.; Jaque, D. Optomagnetic Nanoplatforms for In Situ Controlled Hyperthermia. *Adv. Funct. Mater.* **2018**, *28*, 1704434.
(36) Ebrahimi, M. On the Temperature Control in Self-Controlling Hyperthermia Therapy. *J. Magn. Magn. Mater.* **2016**, *416*, 134−140.
(37) Zhang, W.; Zuo, X.; Niu, Y.; Wu, C.; Wang, S.; Guan, S.; Silva, S. R. P. Novel Nanoparticles with Cr3+ Substituted Ferrite for Self-Regulating Temperature Hyperthermia. *Nanoscale* **2017**, *9*, 13929−13937.
(38) Rabanel, J.-M.; Hildgen, P.; Banquy, X. Assessment of PEG on Polymeric Particles Surface, a Key Step in Drug Carrier Translation. *J. Controlled Release* **2014**, *185*, 71−87.
(39) Burns, N. L.; Van Alstine, J. M.; Harris, J. M. Poly(ethylene glycol) Grafted to Quartz: Analysis in Terms of a Site-Dissociation Model of Electroosmotic Fluid Flow. *Langmuir* **1995**, *11*, 2768−2776.
(40) Khandadash, R.; Machtey, V.; Shainer, I.; Gottlieb, H. E.; Gothilf, Y.; Ebenstein, Y.; Weiss, A.; Byk, G. Novel biocompatible hydrogel nanoparticles: generation and size-tuning of nanoparticles by the formation of micelle templates obtained from thermo-responsive monomers mixtures. *J. Nanopart. Res.* **2014**, *16*, 2796.
(41) Fan, X.; Xiao, J.; Wang, W.; Zhang, Y.; Zhang, S.; Tang, B. Novel Magnetic-to-Thermal Conversion and Thermal Energy Management Composite Phase Change Material. *Polymers* **2018**, *10*, 585.
(42) Liu, X.; Zheng, J.; Sun, W.; Zhao, X.; Li, Y.; Gong, N.; Wang, Y.; Ma, X.; Zhang, T.; Zhao, L. Y.; Hou, Y.; Wu, Z.; Du, Y.; Fan, H.; Tian, J.; Liang, X.-J. Ferrimagnetic Vortex Nanoring-Mediated Mild Magnetic Hyperthermia Imparts Potent Immunological Effect for Treating Cancer Metastasis. *ACS Nano* **2019**, *13*, 8811−25.
(43) Sasikala, A. R. K.; Thomas, R. G.; Unnithan, A. R.; Saravanakumar, B.; Jeong, Y. Y.; Park, C. H.; Kim, C. S. Multifunctional Nanocarpets for Cancer Theranostics: Remotely Controlled Graphene Nanoheaters for Thermo-Chemosensitisation and Magnetic Resonance Imaging. *Sci. Rep.* **2016**, *6*, 20543.
(44) Keblinski, P.; Cahill, D. G.; Bodapati, A.; Sullivan, C. R.; Taton, T. A. Limits of Localized Heating by Electromagnetically Excited Nanoparticles. *J. Appl. Phys.* **2006**, *100*, 054305.
(45) Riedinger, A.; Guardia, P.; Curcio, A.; Garcia, M. A.; Cingolani, R.; Manna, L.; Pellegrino, T. Subnanometer Local Temperature Probing and Remotely Controlled Drug Release Based on Azo-Functionalized Iron Oxide Nanoparticles. *Nano Lett.* **2013**, *13*, 2399−406.
(46) Creixell, M.; Bohorquez, A. C.; Torres-Lugo, M.; Rinaldi, C. EGFR-Targeted Magnetic Nanoparticle Heaters Kill Cancer Cells without a Perceptible Temperature Rise. *ACS Nano* **2011**, *5*, 7124−7129.
(47) *Clinical Magnetic Resonance Imaging*; Edelman, R. R., Hesselink, J. R., Zlatkin, M. B., Eds.; Saunders Publishing Co.: Philadelphia, PA, 1996; p 2196.
(48) Gobbo, O. L.; Wetterling, F.; Vaes, P.; Teughels, S.; Markos, F.; Edge, D.; Shortt, C.; Crosbie-Staunton, C.; Radomski, M. W.; Volkov, Y.; Prina-Mello, A. Biodistribution and Pharmacokinetic Studies of SPION Using Particle Electron Paramagnetic Resonance, MRI and ICP-MS. *Nanomedicine* **2015**, *10*, 1751−1760.
(49) FDA's Center for Drug Evaluation and Research (CDEER). *Guidance for Industry Estimating the Maximum Safe Starting Dose in Initial Clinical Trials for Therapeutics in Adult Healthy Volunteers*, July 2005; Corpus ID: 17535338.
(50) Mahmoudi, K.; Bouras, A.; Bozec, D.; Ivkov, R.; Hadjipanayis, C. Magnetic Hyperthermia Therapy for the Treatment of Glioblastoma: A Review of the Therapy's History, Efficacy and Application in Humans. *Int. J. Hyperthermia* **2018**, *34*, 1316−1328.
(51) Stigliano, R. V.; Shubitidze, F.; Petryk, J. D.; Shoshiashvili, L.; Petryk, A. A.; Hoopes, P. J. Mitigation of Eddy Current Heating During Magnetic Nanoparticle Hyperthermia Therapy. *Int. J. Hyperthermia* **2016**, *32*, 735−748.
(52) Sykes, E. A.; Chen, J.; Zheng, G.; Chan, W. C. Investigating the Impact of Nanoparticle Size on Active and Passive Tumor Targeting Efficiency. *ACS Nano* **2014**, *8*, 5696−5706.
(53) Dai, Q.; Wilhelm, S.; Ding, D.; Syed, A. M.; Sindhwani, S.; Zhang, Y.; Chen, Y. Y.; MacMillan, P.; Chan, W. C. W. Quantifying the Ligand-Coated Nanoparticle Delivery to Cancer Cells in Solid Tumors. *ACS Nano* **2018**, *12*, 8423−8435.
(54) Ganapathy-Kanniappan, S.; Geschwind, J. Tumor Glycolysis as a Target for Cancer Therapy: Progress and Prospects. *Mol. Cancer* **2013**, *12*, 152.

https://doi.org/10.1021/acsanm.1c02676
ACS Appl. Nano Mater. XXXX, XXX, XXX−XXX